

## **Sunquakes of Solar Cycle 24**

Ivan N. Sharykin 1,2 and Alexander G. Kosovichev 3,4 1

Space Research Institute (IKI) of the Russian Academy of Sciences, Profsoyuznaya 84/32, Moscow, 117997, Russia; ivan.sharykin@phystech.edu

Moscow Institute of Physics and Technology, Institutsky Lane 9, Dolgoprudny, Moscow region, 141700, Russia

Department of Physics, New Jersey Institute of Technology, University Heights, Newark, NJ 07102, USA

Center for Computational Heliophysics, New Jersey Institute of Technology, University Heights, Newark, NJ 07102, USA Received 2019 November 16; revised 2020 March 29; accepted 2020 April 12; published 2020 May 27

## **Abstract**

The paper presents results of a search for helioseismic events (sunquakes) produced by M-X class solar flares during Solar Cycle 24. The search is performed by analyzing photospheric Dopplergrams from the Helioseismic Magnetic Imager. Among the total number of 500 M-X class flares, 94 helioseismic events were detected. Our analysis has shown that many strong sunquakes were produced by solar flares of low M class (M1–M5), while in some powerful X-class flares helioseismic waves were not observed or were weak. Our study has also revealed that only several active regions were characterized by the most efficient generation of helioseismic waves during flares. We found that the sunquake power correlates with the maximum value of the soft X-ray flux time derivative better than with the X-ray class, indicating that the sunquake mechanism is associated with high-energy particles. We also show that the seismically active flares are more impulsive than the flares without helioseismic perturbations. We present a new catalog of helioseismic solar flares, which opens opportunities for performing statistical studies to better understand the physics of sunquakes as well as the flare-energy release and transport.

*Unified Astronomy Thesaurus concepts*: Solar flares (1496); Helioseismology (709); Solar x-ray flares (1816); Optical flares (1166)

## 1. Introduction

Strong photospheric perturbations during solar flares are believed to be accompanied by the generation of helioseismic waves, also referred to as "sunquakes." This phenomenon was initially suggested by Wolff (1972), theoretically predicted by Kosovichev & Zharkova (1995), and later discovered by Kosovichev & Zharkova (1998) using Dopplergrams from the Michelson Doppler Imager (MDI) on board the Solar Orbital Heliospheric Observatory (Scherrer et al. 1995). Helioseismic waves are observed in photospheric line-of-sight (LOS) Dopplergrams as concentric (usually highly anisotropic) waves spreading out from the initial photospheric flare impacts observed during the impulsive phase. They represent acoustic waves that travel through the solar convective zone, where the corresponding acoustic rays are curved due to refraction caused by the increase of depth temperature. The acoustic waves emitted into the solar interior are reflected back to the solar surface and observed as traveling circular wave packets in the Dopplergrams. Helioseismic events are usually associated with compact photospheric perturbation and the appearance of continuum emission close to the acoustic sources reconstructed by the helioseismic holography method (Lindsey & Braun 1997; Donea et al. 1999; Lindsey & Braun 2000), see also the statistical work of Buitrago-Casas et al. (2015).

Observational properties and theories of sunquakes can be found in the reviews of Donea (2011) and Kosovichev (2015). We briefly mention hypotheses of the sunquake generation. In particular, the mechanism of the flare-excited helioseismic waves had been considered in the frame of a beam-driven hypothesis, assuming that the initial perturbation is produced by the hydrodynamic response to accelerated electrons injected into the chromosphere (Kosovichev & Zharkova 1995), which is confirmed by the close temporal and spatial association of sunquake sources with hard X-ray emission sources (e.g., Kosovichev 2006; Kosovichev & Sekii 2007;

Sharykin et al. 2017). The backwarming effect of photospheric heating by flare UV radiation may also induce the pressure perturbation needed to generate sunquake waves (Donea 2011). In addition, the plasma momentum can be transferred by a sharp enhancement of pressure gradient due to eruption of a magnetic flux-rope (e.g., Zharkov et al. 2011, 2013) or by an impulse Lorentz force that can be stimulated by changing magnetic fields in the lower solar atmosphere (Hudson et al. 2008; Alvarado-Gómez et al. 2012; Fisher et al. 2012; Burtseva et al. 2015; Russell et al. 2016). Sharykin & Kosovichev (2015) and Sharykin et al. (2015) discussed that rapid dissipation of electric currents in the low atmosphere could also explain sunquake initiation. The exact cause of sunquakes is still unknown.

Perhaps, different sunquake events can be caused by different mechanisms, or, different mechanisms can operate together. In order to understand why some flares produce sunquakes and some do not, and what physical properties lead to the flare seismic activity, it is important to perform statistical studies. Initial catalogs of sunquakes were presented by Buitrago-Casas et al. (2015) and Besliu-Ionescu et al. (2017) for Solar Cycles 23 and 24 (up to 2014 February). These surveys reported 23 and 18 helioseismic events correspondingly and the first work considered only flares with pronounced hard X-ray emission above 50 keV according to the RHESSI (Lin et al. 2002) catalog. More recently, Chen (2019) analyzed 60 strong flares (with the Geostationary Operational Environmental Satellite (GOES) X-ray class greater than M5) in Solar Cycle 24 to search for sunquakes by a helioseismic holography method. A total of 24 flares were found to be seismically active, giving a total of 41 sunquakes. It is worth noting that analyses of flares during Cycle 23 using MDI data found sunquake events only for X-class flares while analysis of Cycle 24 data from HMI data discovered sunquakes for M-class and even a C-class flare (Sharykin & Kosovichev 2015).

In order to obtain a clear understanding of the mechanism of sunquakes and answer various questions (why some flares produce sunquakes and others do not, and how the sunquake power depends on flare properties) it is necessary to carry out statistical studies, the first step of which is to create a comprehensive catalog of the sunquake events. The scope of this work is to perform a search of sunquake events in all M-X class solar flares observed on the solar disk during Solar Cycle 24. We perform the following tasks:

- 1. Develop a comprehensive catalog of sunquake events during Solar Cycle 24.
- 2. Compare helioseismic flares and flares without photospheric disturbances from the point of view of basic parameters that can be extracted from the GOES soft X-ray data (Bornmann et al. 1996), e.g., X-ray class, duration of the impulsive phase, and maximum value of the X-ray flux time derivative.
- 3. Investigate the relationship between the sunquake energy estimated from the acoustic holography technique and the flare X-ray properties from the GOES data.

The X-ray characteristics in these tasks provide the most important parameters of the flare energetics. A series of recent studies of the global energetics of flares and CMEs has found the following overall average ratios:  $51\% \pm 17\%$  for electron acceleration,  $17\% \pm 17\%$  for ion acceleration,  $7\% \pm 14\%$  for CME kinetic energies, and  $7\% \pm 17\%$  for direct heating (Aschwanden et al. 2019). The time derivative of the soft X-ray (SXR) flux is correlated with the hard X-ray (HXR) flux (the Neupert effect) (Neupert 1968; Dennis & Zarro 1993). This is a result of electron beam heating of the chromosphere, where the nonthermal HXR emission is produced by the electron beam (Brown 1971). The beam heats the chromospheric plasma to coronal temperatures causing its evaporation and increase of the SXR emission in the corona, as follows from the radiative hydrodynamics simulations (e.g., Livshits et al. 1981; Fisher et al. 1985; Kosovichev 1986; Allred et al. 2015). Recent helioseismic modeling of sunquakes by Stefan & Kosovichev (2019) showed that at least half the studied events were consistent with the electron beam hypothesis. Therefore, the statistical comparison of the X-ray and helioseismic energetics is an important step to understanding the physical processes associated with the flare helioseismic response.

The paper is divided into five sections. Section 2 describes methods to identify flare helioseismic waves and their sources from the SDO/HMI data. The Section 3 describes a catalog of sunquakes of Solar Cycle 24, and presents a summary of the most seismically active regions. A statistical study of the seismic and nonseismic flares is presented in the Section 4. Section 5 summarizes results and formulates conclusions.

## 2. Identification of Sunquakes and Their Sources

For analysis, we use the HMI LOS Dopplergrams with 45 s cadence and 1" spatial resolution (0."5 px<sup>-1</sup>) (Scherrer et al. 2012). To search for helioseismic waves and their sources we used time sequences of the running difference of derotated (removed effects of solar rotation) Dopplergrams remapped onto the heliographic grid (Figure 1). To isolate the wave signal from convective noise we applied to each pixel of the Dopplergram data cubes a Gaussian frequency filter with a central frequency of 6 mHz and standard deviation width of

2 mHz, which is optimal for rendering the sunquake signal (Donea et al. 1999).

For the search of sunguakes, we consider only solar flares that produced perturbation in the photospheric HMI Dopplergrams. This is justified because sunguakes and their sources appear as photospheric perturbations. First, we visually inspected all Dopplergram series to find Doppler impacts during flares. It is worth noting that we used subjective visual inspection due to the following reason. The initial helioseismic impact usually starts from strong photospheric Doppler perturbations seen during the flare impulsive phase. However, it is very difficult to characterize these perturbations quantitatively (e.g., amplitude value) due to the Fe I line shape distortions not allowing us to reliably determine the LOS velocity associated with this impact (Raja Bayanna et al. 2014; Sun et al. 2017). This can be done in the frame of a future separate work following the forward modeling approach (Sadykov et al. 2020). At this stage of the work (statistical survey of the flare seismicity), we include only events with the impacts during the flare impulsive phase, which can be visually identified in the HMI Dopplergrams above the noise level. We generated running time-difference Doppler movies for all flares and found 181 events with the Doppler impacts of different magnitudes. Then, we used three approaches to find helioseismic waves in the selected flares:

- 1. Create movies showing time sequences of running differences of derotated HMI Dopplergrams projected onto the heliographic grid and filtered in the frequency range of 5–7 mHz. The helioseismic waves are detected by visual inspection of these movies.
- Select photospheric impacts detected in the HMI Dopplergrams (also derotated, reprojected and filtered), and construct time-distance (TD) diagrams. The helioseismic waves are detected in the form of a characteristic ridge pattern in the TD diagrams (Kosovichev & Zharkova 1998).
- 3. Reconstruct the two-dimensional structure of seismic sources by using the helioseismic holography method (Lindsey & Braun 2000). This approach employs a theoretical Green function of helioseismic waves to calculate the egression acoustic power corresponding to the observed Doppler velocity perturbations.

The most direct way to find sunquake waves is visual inspection of the Dopplergrams movies (the SQ movie method). Generally, the sunquake ripples appear about 10–15 minutes after the initial impact. The excited helioseismic waves travel beneath the solar surface before they appear on the surface in the form of sunquake ripples. The travel distance and travel times are shorter for the waves with shorter horizontal wavelengths. However, such waves in the sunquake signal are strongly damped (Stefan & Kosovichev 2019). In addition, the sunquake ripples usually are not observed when they travel in strong magnetic field regions (sunspot umbra and penumbra) due to the wave absorption (Zhao & Chou 2016) and reflection in deeper subsurface layers (Zhao et al. 2012). While the visual inspection provides the most unambiguous detection in the case of strong sunquakes, and allows us to estimate the wave anisotropy and track propagation through the active region, it becomes subjective in the case of weak events. The problem is that in addition to the random oscillation background, there are many sporadic weak acoustic sources that can be

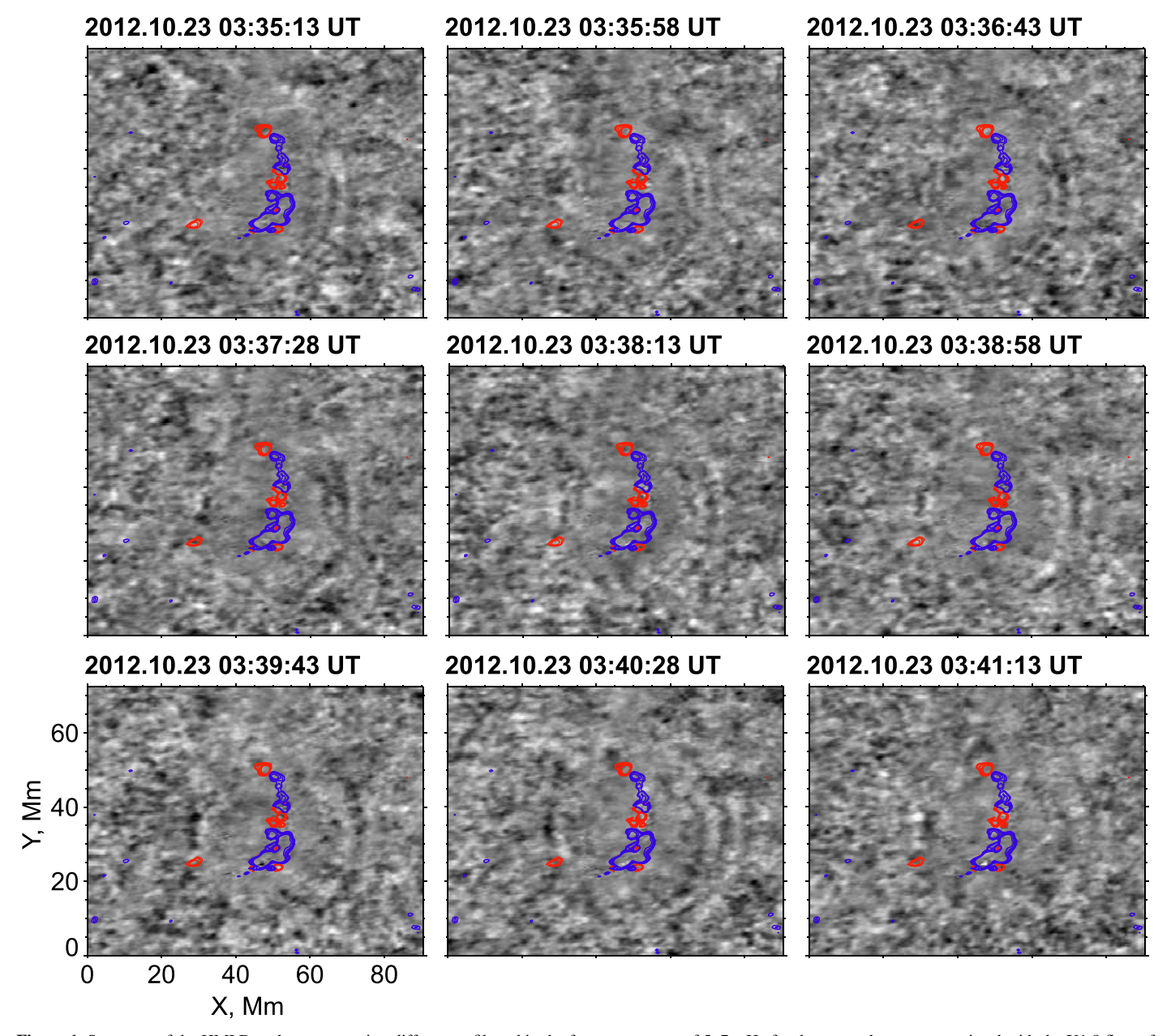


**Figure 1.** Sequence of the HMI Dopplergram running differences filtered in the frequency range of 5–7 mHz for the sunquake event associated with the X1.8 flare of 2012 October 23. Red and blue contours highlight regions of strong upward and downward velocity perturbations with the absolute value higher than 1 km s<sup>-1</sup>.

misinterpreted as sunquakes. We identify only unambiguous events as helioseismic when circular-shape wave packets are spreading out from initial photospheric impacts, as shown Figure 1 (similarly to the ripples that appear when a pebble is dropped into water). Such wave packets are usually well seen in the active region areas where acoustic background amplitude is suppressed due to magnetic field.

The other two methods, TD and acoustic holography, are less subjective, but depend on the model of the solar interior structure and theory of helioseismic waves. The helioseismic waves can be identified as a characteristic ridge in the TD diagram that shows the wave signal averaged for given distances around a reference (wave source) point. This point is selected in the area of the initial photospheric flare disturbances and the strongest acoustic sources deduced by the acoustic holography. We construct two types of the TD diagrams. The first one is obtained by circular averaging. In this

case, for each time moment (on the time axis of the TD diagram) we calculate a one-dimensional distribution of the Dopplergram signal obtained by averaging it along circles with radii equal to the distances (on the distance axis of the TD diagram) from 0 to 50 Mm. Another type of TD diagram, which is used for highly anisotropic wave fronts, is obtained by averaging the signal over sectors. The sectoral TD diagrams are calculated for the angular range covering  $\pi/4$  for distances from 0 to 50 Mm. The sector direction is selected to find the strongest helioseismic signal with a step of  $\pi/8$  (so we investigate 16 TD diagrams for each event). To make the conclusion that the observed wave pattern in the TD diagram corresponds to a sunquake event we compare it with the theoretical TD relation calculated in the ray approximation for a standard solar interior model (Christensen-Dalsgaard et al. 1993). It is marked by a dashed curve in the TD diagrams in Figure 2. The position of the wave ripples in the TD diagram

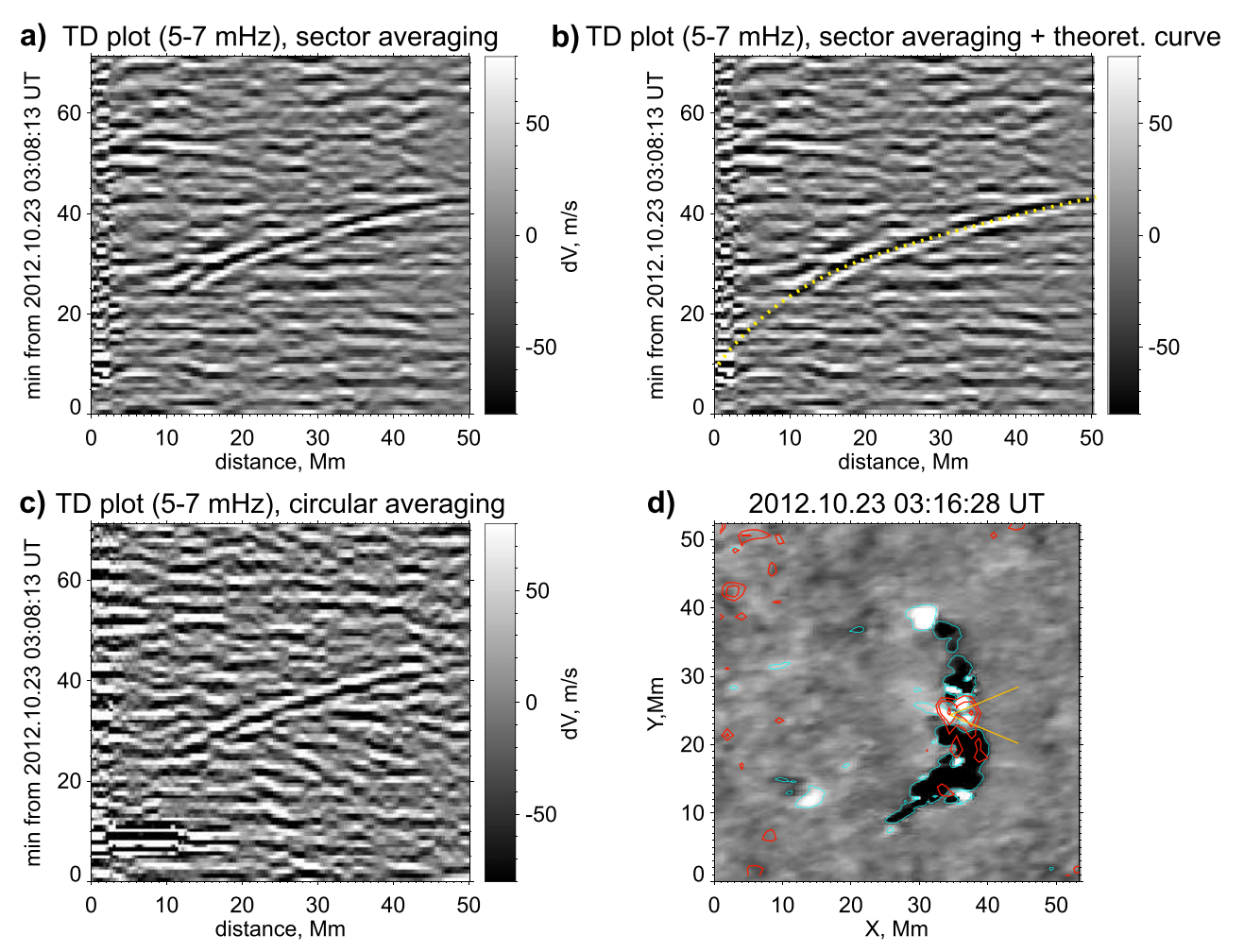


**Figure 2.** Time–distance (TD) diagrams in the frequency range of 5–7 mHz for the sunquake event associated with the X1.8 flare of 2012 October 23. Panels (a) and (b) show the TD diagram for the case of sector averaging around a point selected in the region of a strong photospheric perturbation and the acoustic source deduced by the acoustic holography method. The sector and selected source point are shown by yellow lines in panel (d). The yellow dotted line in panel (b) corresponds to the ray-theoretical prediction of the helioseismic wave path. Panel (c) shows the TD diagram obtained from Dopplergram averaging over the full circle. Panel (d) presents the photospheric Dopplergram difference map (white–black background image) filtered in the frequency range of 5–7 mHz with overplotted red contours (30%, 50%, and 90% levels relative to maximum value) highlighting the acoustic sources deduced from acoustic holography. Cyan contours show regions with the absolute value of velocity perturbation higher than 200 m s<sup>-1</sup>.

fits to the theoretical model. Thus, the observed wave was generated in the source corresponding to the Dopplergram disturbance around the selected reference point.

The helioseismic holography method (Lindsey & Braun 1997; Donea et al. 1999; Lindsey & Braun 2000) is based on the idea of using a theoretical model of helioseismic waves to reconstruct the two-dimensional distribution of acoustic sources. This approach uses a theoretical Green function of helioseismic waves for the standard solar interior model to calculate the egression acoustic power corresponding to the Doppler velocity perturbations. An example of the egression acoustic power map calculated in the frequency range of 5–7 mHz is shown in Figure 4. We calculated this map by summing up the egression acoustic power snapshots within a time interval found from the uncertainty principle:  $\Delta t \sim 1/\Delta \nu \approx 500~\text{s}$ , where  $\Delta \nu = 2~\text{mHz}$ . This time interval corresponds to the appearance of strong Doppler velocity perturbations. The egression power map is compared with the corresponding Dopplergram.

Figures 4 and 5 illustrate the acoustic holography method applied to two different flares. In these figures, we present the acoustic egression power maps constructed from five 45 s snapshots of the 225 s duration, which is approximately equal

to  $\Delta t/2 = 1/(2\Delta\nu) = 250$  s. Figure 4 presents a very strong sunquake event during X1.8 solar flare of 2012 October 23. This event is an example of the flare with an obvious helioseismic impact seen in the egression power maps. In this case, all three methods provide a robust detection: the Dopplergram movie revealed very clear wave ripples, and the TD analysis (see more details in the text below) confirmed that these waves were acoustic and spread from the initial photospheric perturbations. We show the photospheric flare impacts for one time moment in the corresponding frequency-filtered Dopplergram time-difference in Figure 4(b) and, also, indicate them for three time moments by white contours overlaid on the acoustic power maps in panels (c2)–(e2).

The advantage of the helioseismic holography technique is that it provides a quantitative estimation of the strength of the sunquake source. After analysis of many helioseismic events we decided to use the following criteria for detecting sunquakes by this technique. First of all, the reconstructed acoustic sources have to be in the area of the initial photospheric perturbations, usually observed during the flare impulsive phases. Other important criteria are the magnitude and timing of the total helioseismic signal. If the acoustic power spatially integrated over the area that

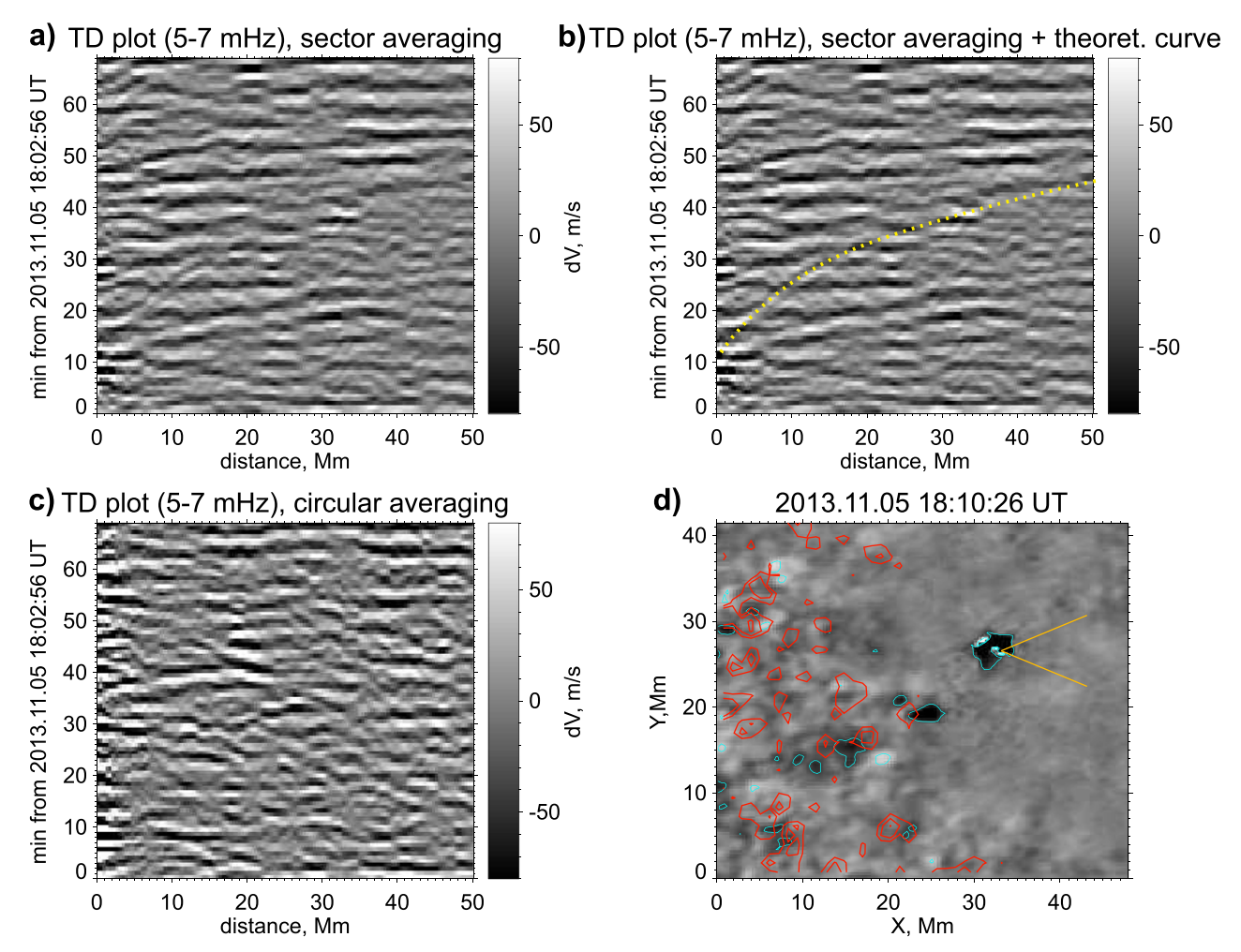


**Figure 3.** Time–distance diagrams in the frequency range of 5–7 mHz for the sunquake event associated with the M1.0 flare of 2013 November 5. This flare is an example of weak sunquake events found in the Dopplergram movie with weak wave signals seen in the TD diagram and the egression power map deduced from the acoustic holography. Panels (a)–(d) show the same properties as in Figure 2.

includes the photospheric perturbations and acoustic sources (shown by dashed contours in Figures 4(b)–(g)) exceeds three background noise levels (calculated for a time period before appearance of the photospheric impacts), then we identify the signal as a helioseismic event. We also introduce a special class of helioseismic event candidates for the cases when weak acoustic sources are observed around photospheric perturbations in the Dopplergrams, but the calculated acoustic power is below the  $3\sigma$  background level. Such a weak event observed during M1.0 flare of 2013 November 5, is demonstrated in Figure 5. In this case, the holography method does not provide a clear detection. It is worth noting that the existence of sunquake waves in this flare was verified by the SQ movies and the TD diagram. We identified the holography signals as sunquake candidates only in the case of nondetection of waves in the movie and in the TD plot.

Figures 2 and 3 demonstrate examples of the TD diagrams for the flares for which the acoustic holography results were summarized in Figures 4 and 5. For the X1.8 flare we have a clear wave signal in the TD diagrams for both types: the sectoral (a)–(b) and circular (c) averaging. Considering the weak M1 flare of 2013 November 5 in Figure 3, we found the sunquake signal only for the sector in the direction shown by yellow lines in panel (d).

All analysis methods described in this section have been employed to find sunguakes and possible candidates in all M-X class flares with photospheric perturbations. In the next section we present results of this search.

## 3. Catalog of Sunquakes

Our results of searching for sunquakes among the M-X class flares with photospheric disturbances are presented in Table 1. The first four columns show the basic information about flares: date, GOES class, NOAA number, and angular position on the solar disk. The next three columns show results of identification of helioseismic waves. Plus or minus signs mean positive or negative identification using the three methods discussed in the previous section. The question marks indicate the potential candidates deduced from the holography method.

A summary of the catalog shown in Table 1 is the following:

- 1. Total number of the analyzed M- and X-class flares from 2011 February 13 to 2017 September 8: 507.
- 2. Total number of flares with photospheric perturba-
- 3. Total number of helioseismic events registered by each of the three methods: 62 (movie method), 80 (holography method), 81 (TD method) (+29 candidates deduced from holography method).
- 4. Total number of sunquakes detected by all three methods: 54.

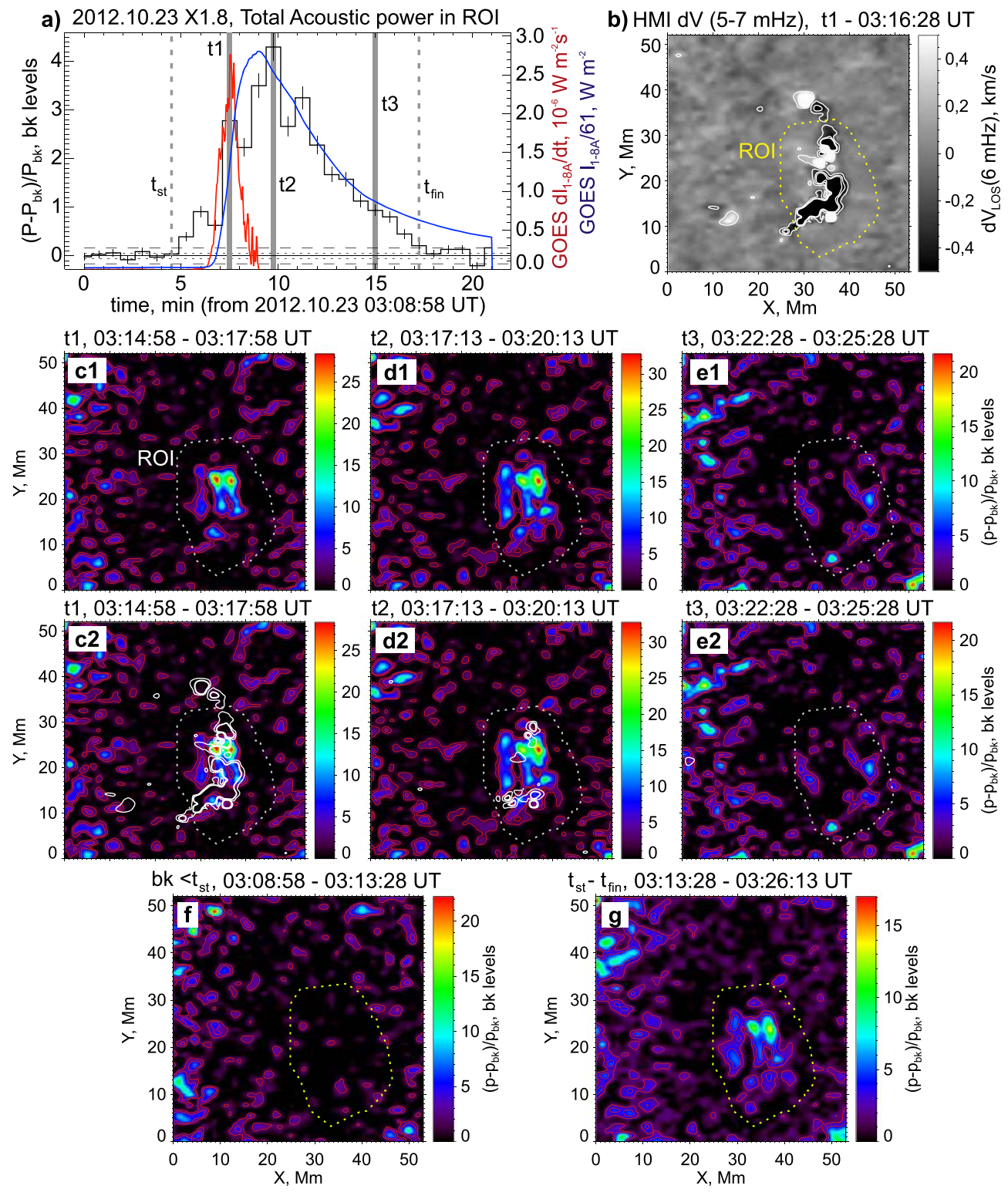


**Figure 4.** Evolution of sunquake impacts investigated by acoustic holography in the frequency range of 5–7 mHz for X1.8 flare of 2012 October 23. The black histogram in panel (a) shows the total acoustic power flux (in units of background flux) within the region of interest (ROI) shown by the dashed contours in other panels. The sunquake signal is marked between two vertical lines with labels  $t_{st}$  and  $t_{fin}$ . Blue and red curves correspond to GOES 1–8 Å flux and its time derivative. For the purpose of visualization the GOES flux is divided by a factor written in the axis title to match to maximum value of its time derivative. Panel (b) shows the photospheric Dopplergram difference map (white–black background image) filtered in the frequency range of 5–7 mHz for time moment t1 (first vertical gray line in panel (a)). Three gray vertical lines (marked as t1-3) in panel (a) correspond to three time moments selected to demonstrate the acoustic sources in the holography images shown in panels (c)–(e). Panels with labels 1 and 2 show the same acoustic egression maps. Contours in panels (c2)–(e2) highlight regions with the absolute value of velocity perturbation higher than 200 m s<sup>-1</sup>. Panels (f) and (g) show the integrated (sunquake signal between  $t_{st}$  and  $t_{fin}$ ) and background (signal before  $t_{st}$ ) acoustic egression map, respectively.

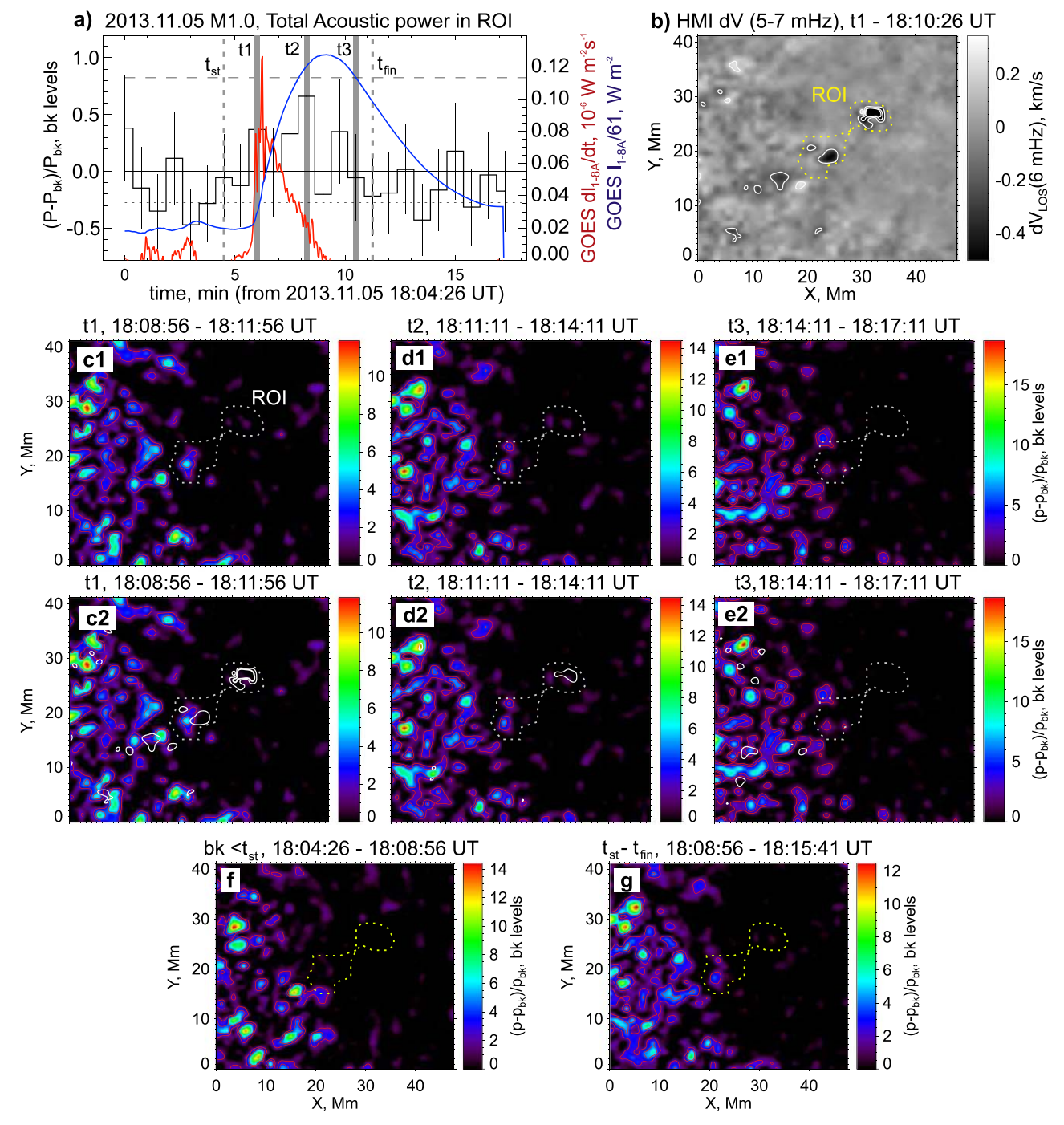


Figure 5. Evolution of sunquake impacts investigated by acoustic holography in the frequency range of 5–7 mHz for M1.0 of 2013 November 5. Panels (a)–(g) show the same properties as in Figure 4.

- 5. Total number of sunquakes detected by at least one method: 94 (+20 candidates) = 114 sunquakes. This means that more than half of the flares with photospheric perturbations are accompanied by helioseismic response.
- 6. Total number of active regions that produced sunquakes: 35.
- 7. Eight of these active regions produced more than 60% of sunquakes (> 5 events/AR).

Our statistical analysis confirmed the complexity of the sunquake phenomenon discussed in the previous works briefly discussed in Section 1. First of all, we often observed sunquakes in relatively weak (low M class) events. Sometimes, the helioseismic sources in low M-class flares were more powerful than in X-class flares. Moreover, there were X-class flares without any manifestations of helioseismic response. We found many sunquakes during flares that occurred close to the solar limb: 31 and 9 events were at the angular distances from the disk center > 700 and >800", respectively. Previously, it was thought that it is hard to observe helioseismic waves close to the limb because of the small amplitude of the LOS Doppler

Table 1
Catalog of Sunquake Events and Acoustic Sources

Date UT Time	GOES Class	AR NOAA	Location (arcseconds)	Movie Method	Holography Method	TD Method	$ H_{+} ^{2}$ (10 <sup>26</sup> erg)	$S_{\text{max}}$ (10 <sup>17</sup> cm <sup>2</sup> )	$\frac{df/dt(1-8 \text{ Å})}{(10^{-7} \text{ W m}^{-2} \text{ s}^{-1})}$
2011 Feb 13 17:28	M6.6	11158	211		?		3.0	4.4	5.8
2011 Feb 14 17:20	M2.2	11158	278		?		3.4	2.9	3.8
2011 Feb 15 01:44	X2.2	11158	319	+	+	+	10.6	9.6	10.5
2011 Feb 18 09:55	M6.6	11158	809	+	+	+	12.4	9.0	12.2
2011 Feb 18 12:59	M1.4	11158	808		+	+	4.2	3.7	2.1
2011 Mar 14 19:30	M4.2	11169	733		+		12.4	11.1	7.6
2011 Mar 15 00:18	M1.0	11169	761		?		6.3	4.9	3.0
2011 Jul 30 02:04	M9.3	11261	493	+	+	+	33.2	15.0	14.8
2011 Sep 6 22:12	X2.1	11283	299		?		0.6	0.8	27.4
2011 Sep 7 22:32	X1.8	11283	496	+	+	+	9.9	9.1	24.8
2011 Sep 9 12:39	M1.2	11283	708		?		5.1	6.6	1.1
2011 Sep 24 20:29	M5.8	11302	709		+	+	5.6	5.9	6.3
2011 Sep 25 02:27	M4.4	11302	676		?	+	3.5	4.9	3.9
2011 Sep 25 08:46	M3.1	11302	640	+	+	+	4.0	5.6	4.2
2011 Sep 26 05:06	M4.0	11302	526	+	+	+	14.7	12.3	6.0
2011 Oct 2 17:19	M1.3	11302	749	+	+	+	18.8	6.8	3.1
2011 Nov 3 20:16	X1.9	11339	842	+	+	+	27.1	19.3	19.8
2011 Nov 5 20:31	M1.8	11339	577		+		8.7	7.4	2.7
2011 Dec 25 18:11	M4.0	11387	462		?	+	4.2	3.0	6.6
2011 Dec 30 3:03	M1.2	11389	812		+	+	6.4	4.1	1.6
2011 Dec 31 13:09	M2.4	11389	607		?		1.1	1.1	4.9
2012 Mar 5 19:10	M2.1	11429	724		+		6.0	12.2	3.7
2012 Mar 5 19:27	M1.8	11429	724		+	+	1.5	5.4	3.0
2012 Mar 5 22:26	M1.3	11429	705		?		1.7	4.6	2.0
2012 Mar 6 04:01	M1.0	11429	674		+	+	0.5	2.0	0.8
2012 Mar 6 07:52	M1.0	11429	654		+	+	2.0	5.3	0.9
2012 Mar 6 12:23	M2.1	11429	643		+	+	0.6	1.6	1.5
2012 Mar 7 00:02	X5.4	11429	570		+	+	4.6	9.1	13.7
2012 Mar 9 03:22	M6.3	11429	380	+	+	+	14.5	10.3	2.7
2012 May 8 13:02	M1.4	11476	636		+	+	1.7	3.3	1.8
2012 May 9 12:21	M4.7	11476	466		?	+	14.7	7.7	3.0
2012 May 9 14:02	M1.8	11476	452		?		1.0	4.0	1.7
2012 May 9 21:01	M4.1	11476	397	+	+	+	10.2	7.3	5.3
2012 May 10 04:11	M5.7	11476	341	+	+	+	10.0	10.1	7.7
2012 May 10 20:20	M1.7	11476	246		?	+	6.1	4.7	1.5
2012 Jul 4 09:47	M5.3	11515	426	+	+	+	11.7	8.7	5.9
2012 Jul 4 12:07	M2.3	11515	446	+		+			
2012 Jul 4 14:35	M1.3	11515	454	+	+	+	5.1	7.3	1.7
2012 Jul 5 01:05	M2.4	11515	509	+	+	+	3.1	4.7	1.6
2012 Jul 5 03:25	M4.7	11515	519	+	+	+	10.2	12.9	12.5
2012 Jul 5 06:49	M1.1	11515	538	+		+			
2012 Jul 5 10:44	M1.8	11515	558	+	+	+	1.3	4.2	2.4
2012 Jul 5 11:39	M6.1	11515	568	+	+	+	20.4	19.7	10.9
2012 Jul 5 20:09	M1.6	11515	608	+	+	+	9.3	6.6	3.9
2012 Jul 6 01:37	M2.9	11515	639	+	+	+	9.6	9.6	4.1
2012 Jul 6 13:26	M1.2	11515	721	+	+	+	2.6	2.9	2.4
2012 Jul 6 23:01	X1.1	11515	765	+	+	+	8.1	7.3	11.6
2012 Jul 7 03:10	M1.2	11515	782		+		4.0	6.6	0.8
2012 Jul 7 10:57	M2.6	11515	820		?		2.3	6.2	2.8
2012 Jul 9 23:03	M1.1	11520	610	+	+	+	3.1	7.8	3.7
2012 Oct 23 03:13	X1.8	11598	789	+	+	+	47.1	18.5	27.7
2013 Jan 13 00:45	M1.0	11652	478		+		3.3	3.7	2.5
2013 Jan 13 08:35	M1.7	11652	508		+	+	4.0	2.5	3.9
2013 Feb 17 15:45	M1.9 <sup>a</sup>	11675	473	+	+	+	3.6	2.7	10.1
2013 Apr 22 10:22	M1.0	11726	478		?		1.7	3.4	2.2
2013 Aug 17 18:16	M3.3	11818	505		?		2.7	2.8	3.4
2013 Oct 24 10:30	M3.5	11875	285	+	+	+	3.7	3.6	5.3
2013 Nov 3 05:16	M5.0	11884	319		?		7.4	5.1	6.5
2013 Nov 5 18:08	M1.0	11890	625	+	?	+	0.02	1.6	1.3
2013 Nov 5 22:07	X3.3	11890	600	+	+	+	31.7	17.6	70.4
2013 Nov 6 13:39	M3.8	11890	481	+	+	+	12.4	11.6	4.4
2013 Nov 7 03:34	M2.3	11890	385	+	+	+	6.1	6.7	2.0
2013 Nov 7 14:15	M2.4	11890	304	+	?	+	4.7	4.0	2.5
2013 Nov 8 04:20	X1.1	11890	212	+	+	+	21.4	14.9	21.5

Table 1 (Continued)

(Continued)									
Date UT Time	GOES Class	AR NOAA	Location (arcseconds)	Movie Method	Holography Method	TD Method	$ H_{+} ^{2}$ (10 <sup>26</sup> erg)	$S_{\text{max}} (10^{17} \text{ cm}^2)$	$\frac{df/dt(1-8 \text{ Å})}{(10^{-7} \text{ W m}^{-2} \text{ s}^{-1})}$
2013 Nov 10 05:08	X1.1	11890	328	+	+	+	31.1	20.2	12.7
2013 Nov 17 05:06	M1.0	11900	703		?		5.1	2.8	2.4
2013 Dec 22 15:06	M3.3	11928	807		+		10.4	3.9	2.1
2014 Jan 7 10:07	M7.2	11944	93	+	+		8.6	10.4	12.5
2014 Jan 30 06:33	M2.1	11967	750	·	?		1.3	2.1	2.3
2014 Feb 2 06:24	M2.6	11968	342	+	+	+	7.4	4.2	2.6
2014 Feb 4 03:57	M5.2	11967	248	+	+	+	7.9	9.2	7.4
2014 Feb 7 10:25	M1.9	11968	799	+	+	+	17.0	8.3	8.2
2014 Feb 16 09:20	M1.1	11977	109	+	+	+	3.4	2.6	2.1
2014 Mar 29 17:35	X1.0	12017	525	'	+	'	5.7	5.5	13.7
2014 May 8 09:59	M5.2	12056	728	+	+	+	2.8	5.1	2.9
2014 Jun 11 05:30	M1.8	12080	633		?	т	6.5	6.3	2.6
2014 Juli 11 03.30 2014 Oct 20 09:00	M3.9	12192	626		?		0.5	4.3	2.1
		12192			?	+		7.0	2.3
2014 Oct 20 18:55	M1.4		553	+			10.5		
2014 Oct 22 01:16	M8.7	12192	388	+	+	+	5.4	16.1	2.1
2014 Oct 22 14:02	X1.6	12192	290	+	+	+	1.7	5.5	4.3
2014 Oct 23 09:44	M1.1	12192	226		+	+	1.9	7.3	1.1
2014 Oct 26 18:07	M4.2	12192	667	+	+	+	3.0	8.3	3.0
2014 Nov 9 15:24	M2.3	12205	297		+	+	8.7	8.7	2.4
2014 Nov 15 20:38	M3.7	12209	713		?		3.6	3.7	5.0
2014 Dec 20 00:11	X1.8	12242	502	+	?	+	3.5	12.6	6.6
2015 Jan 3 09:40	M1.1	12253	267	+	+	+	4.3	5.6	1.6
2015 Jan 30 12:10	M2.4	12277	797		+		9.2	7.8	2.4
2015 Mar 10 03:19	M5.1	12297	588	+	+	+	12.5	11.2	7.7
2015 Mar 10 23:46	M2.9	12297	442		+		8.1	8.0	5.1
2015 Mar 11 16:11	X2.1	12297	333		+	+	2.6	4.6	12.2
2015 Mar 12 04:41	M3.2	12297	245		+	+	4.3	5.4	4.5
2015 Mar 12 13:50	M4.2	12297	186		?	+	3.1	3.5	2.3
2015 Mar 12 21:44	M2.7	12297	168		?		3.5	4.8	3.4
2015 Mar 15 09:36	M1.0	12297	502	+	+	+	3.6	6.1	-
2015 Jun 21 09:38	M3.8	12367	807		?		7.4	5.4	6.6
2015 Jun 25 08:02	M7.9	12371	653	+	+	+	7.6	8.7	13.1
2015 Aug 22 21:19	M3.5	12403	376	+	+	+	18.1	14.3	5.1
2015 Aug 24 07:26	M5.6	12403	377		?		5.3	5.7	8.9
2015 Aug 24 17:40	M1.0	12403	417		+		5.3	5.0	2.7
2015 Sep 28 14:53	M7.6	12422	535	+	+	+	20.5	15.9	10.7
2015 Sep 29 06:39	M1.4	12422	622	+	·	+			
2015 Sep 30 13:18	M1.1	12422	766	+	+	+	8.3	4.1	3.9
2015 Oct 1 13:03	M4.5	12422	866	·	+	·	3.6	3.3	4.1
2015 Oct 31 17:48	M1.0	12443	698		+		4.5	5.4	2.8
2017 Sep 4 15:11	M1.5	12673	294		?		6.9	9.9	1.7
2017 Sep 4 20:28	M5.5	12673	341	_		_	2.2	5.0	4.6
2017 Sep 5 01:03	M4.2	12673	349	+ +	+	+	2.5	4.6	6.2
2017 Sep 5 01.03 2017 Sep 6 08:57	X2.2	12673	575	+	+		9.0	28.2	-
2017 Sep 6 08.57 2017 Sep 6 11:53	X2.2 X9.3	12673	599			+	58.9	42.4	63.1
•				+	+	+			
2017 Sep 7 04:59 2017 Sep 7 10:11	M2.4	12673	694 751	+	+	+	9.2	13.2	5.4
•	M7.3	12673	751	+	+	+	24.9	12.8	33.5
2017 Sep 7 14:20	X1.3	12673	747	+	+	+	24.7	23.6	14.3
2017 Sep 8 02:19	M1.3	12673	788	+	+	+	4.9	9.2	2.9
2017 Sep 8 07:40	M8.1	12673	816	+	+	+	9.9	9.6	7.9

Notes. The first five columns show general information about the flare: flare start time (UT), GOES class, and standard active region number from the NOAA database (AR NOAA), angular distance from the disk center. The last three columns present information about seismic transients during the corresponding solar flares. A plus symbol in column "SQ movie method" represents the presence or absence of sunquake waves in the movies made from the frequency-filtered running time differences of the HMI Dopplergrams. A plus symbol in column "TD method" means that we found the characteristic sunquake wave pattern in the time–distance diagram. A plus symbol in column "holography method" means the presence or absence of statistically significant acoustic sources determined by the acoustic holography method. A question mark "?" indicates events as sunquake candidates, which means that there was a weak acoustic signal around the velocity impact sites during the flare, but the acoustic power was below the  $3\sigma$  background noise level. The next three columns  $|H_+|^2$ ,  $S_{\text{max}}$ , and df/dt(1-8) show information about total sunquake energy, area of acoustic sources and maximum values of the GOES SXR flux time derivative (energy release rate). The online version of this catalog is available at https://solarflare.njit.edu/sunquakes/sunquakes.html.

<sup>&</sup>lt;sup>a</sup> The flare of 2013 February 17 is classified as a M1.9 GOES-class flare according to the strongest secondary X-ray peak. However, the sunquake event was associated with the first C7.0 peak (Sharykin & Kosovichev 2015).

NOAA AR	$N_{ m MX}$	$N_{ m dV}$	$N_{ m SQ}$	$N_{ m TD}$	$N_{ m AH}$	$N_{ m All}$	$N_1$	$N_1/N_{ m MX}$
11302	19(1)	7	3	5	4(1)	3	5	0.26
11429	15(1)	11	1	6	7(1)	1	7	0.47
11476	6(0)	6	2	5	3(3)	2	5	0.83
11515	27(1)	17	12	12	11(1)	10	13	0.48
11890	8(3)	8	7	7	5(2)	5	7	0.88
12192	26(5)	12	4	5	4(2)	3	6	0.23
12297	19(1)	9	2	5	5(2)	2	6	0.32
12673	24(3)	18	9	9	9(1)	9	9	0.38
Total	144(15)	88	40	54	48(13)	35	58	
Total in catalog	181(25)	181	62	80	81(29)	54	94	

 Table 2

 Characteristics of Active Regions that Produced Five or More Sunquakes

**Note.**  $N_{\rm MX}$  is the total number of M and X on-disk solar flares in the active regions.  $N_{\rm dV}$  is the total number of flares with Doppler velocity impacts.  $N_{\rm SQ}$ ,  $N_{\rm TD}$ , and  $N_{\rm AH}$  are the numbers of sunquake events detected by using the sunquake movie, the time-distance diagram and the acoustic holography methods, respectively.  $N_{\rm AH}$  is the total number of sunquake events detected by all three methods, and  $N_{\rm 1}$  is the number of sunquakes detected by at least one method. Ratio  $N_{\rm 1}/N_{\rm MX}$  defines the seismic efficiency of AR. The last two rows summarize the sunquake efficiency numbers.

velocity variations due to the projection effect and foreshortening. It is worth noting that morphology of the acoustic sources can be quite complicated representing compact acoustic sources, diffusive large-scale sources, groups of distant compact sources, or a combination of these three types. This reflects the complexity of physical mechanisms responsible for generation of sunquake waves, and flare-energy release. In this work, we will not discuss in detail this classification because it requires further studies of individual events to develop more clear quantitative criteria.

One of the most interesting findings is that we were able to distinguish active regions that gave the largest contribution to the total number of sunguakes. In Table 2 we present a summary of the most "helioseismically efficient" active regions that produced five or more sunquakes. All these active regions had a complex magnetic structure, and were characterized by the Hale class of  $\beta\gamma\delta$ . The largest number of sunquakes was generated in AR 12673 during 2017 September 4-7. It is also worth mentioning that this active region produced the strongest sunquake (ever observed during Cycle 24) during the X9.3 solar flare of 2017 September 6 12:53 UT (Sharykin & Kosovichev 2018). We define a relative seismic efficiency as ratio  $N_1/N_{\rm MX}$ , where  $N_{\rm MX}$  is the total number of M and X solar flares in an active region, observed on the disk, and  $N_1$  is the total number of sunquake events detected at least by one method (without candidates). According to this definition, AR 11890 was the most seismically efficient.

# 4. Results of Statistical Analysis of Sunquake and GOES X-Ray Data

The presented catalog opens opportunities for statistical studies of the sunquake phenomenon. In this paper, we present the initial results of our investigation of the relationship between the acoustic energy of sunquakes and the flare characteristic derived from the soft X-ray (SXR) data obtained from the GOES satellite (Bornmann et al. 1996). In addition, we compare the X-ray characteristics of flares that produced helioseismic signals and flares without photospheric perturbations. In this study, we do not consider potential candidates.

We use the following formula to estimate the total sunquake power  $H_{+}(\text{erg s}^{-1})$  in the frequency range 5–7 mHz:

$$H_{+} = \int_{S_{\text{ROI}}} \int_{t_1}^{t_2} c_s \frac{\rho \delta v^2}{2} dS dt.$$

Here  $S_{\rm ROI}$  means the area of regions of interest where we observed photospheric perturbations and acoustic sources deduced by the holography technique;  $t_{\rm st}$  and  $t_{\rm fn}$  are times of the onset and end of a sunquake event, defined as the time moments when the total acoustic power is above the  $3\sigma$  level of the background noise (see examples in Figures 4(a) and 5(a)). The background noise is determined as the spatially and temporary averaged value of the acoustic preflare power in the region of interest (ROI shown by dashed contours in Figures 4(b)–(g) and 5(b)–(g)). The acoustic energy flux is calculated as  $c_s \rho \delta v^2/2$ , where  $c_s$  is the photospheric sound speed, and  $\delta v$  is the amplitude of acoustic perturbations.

Figure 6 presents two statistical plots: (a) comparison of the total sunquake power with the corresponding maximum value of the GOES SXR flux time derivative, and (b) comparison with the maximum value of the GOES SXR flux in the wavelength band of 1-8 Å. We show the error bars for the sunquake power considering only the acoustic background. Potential systematic uncertainties related to deviations of the solar interior structure from the standard model are not taken into account in these estimates. Colors in Figure 6 highlight flares of the different GOES-class ranges: M- and X-class flares (black), higher than M5.0 (blue), and X-class flares (red). These plots reveal positive linear correlations for both comparisons. However, the maximum value of the SXR flux time derivative shows significantly better correlation with the sunquake energy (the correlation coefficient is 0.69–0.75 for the different GOESclass ranges) than with the peak SXR value (the correlation coefficient is 0.14–0.52). This means that the total helioseismic energy is mostly related to the flare-energy release rate. In other words, flares that are more impulsive are also more seismic.

To compare properties of the flares with and without sunquake events, in Figures 7 and 8 we plot histograms for three groups: (1) seismically active solar flares (red); (2) flares with photospheric perturbations including sunquakes (blue); and (3) flares without photospheric impacts (black). Figure 7

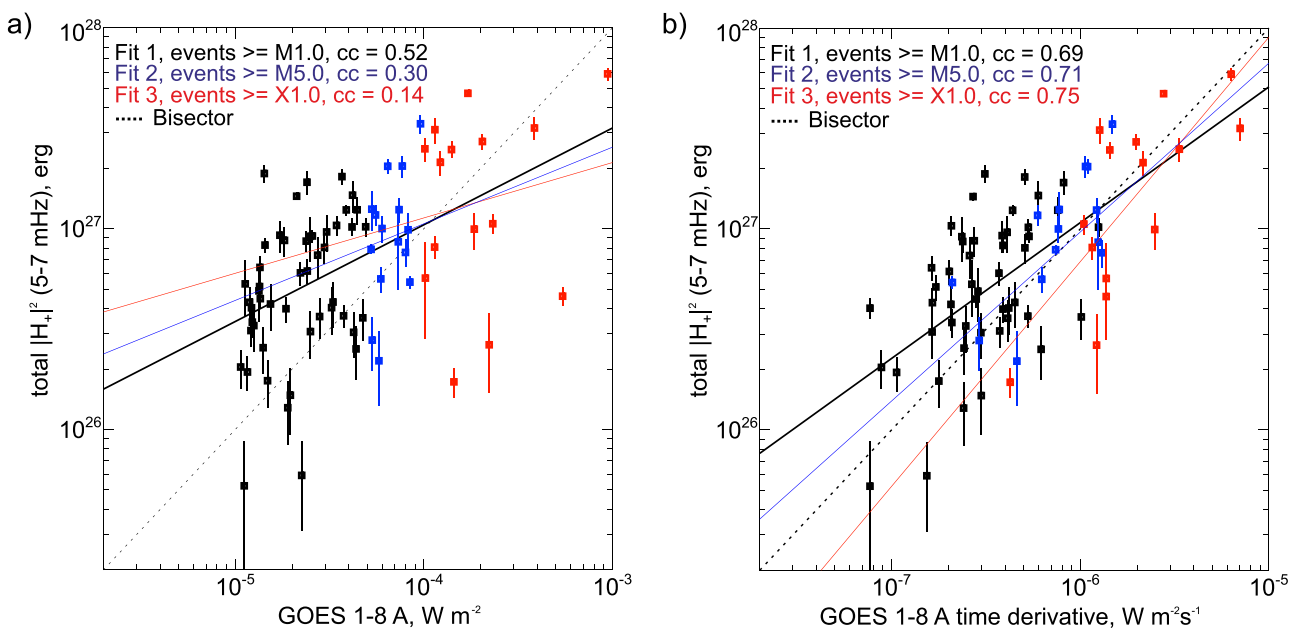


Figure 6. Relationship between the total acoustic energy  $(|H_+|^2)$  in the frequency range 5–7 mHz and the soft X-ray (SXR) flux (a), and maximum value of the SXR time derivative (b). Linear correlation coefficients are written within panels for three flare classes: (1) flares with the SXR class higher than M1.0, (2) higher than M5.0, and (3) only X-class events. The bisector dashed line is also plotted.

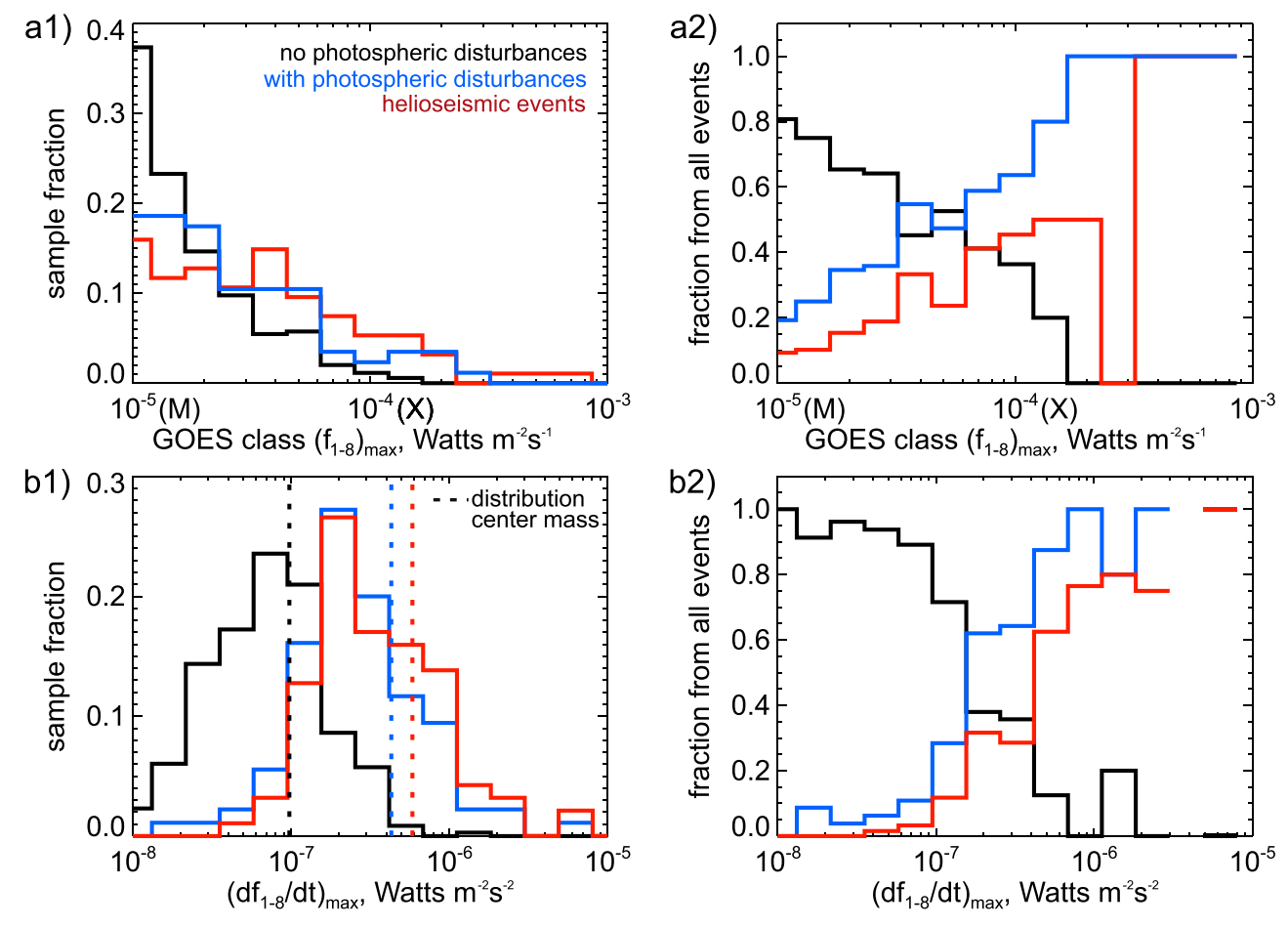
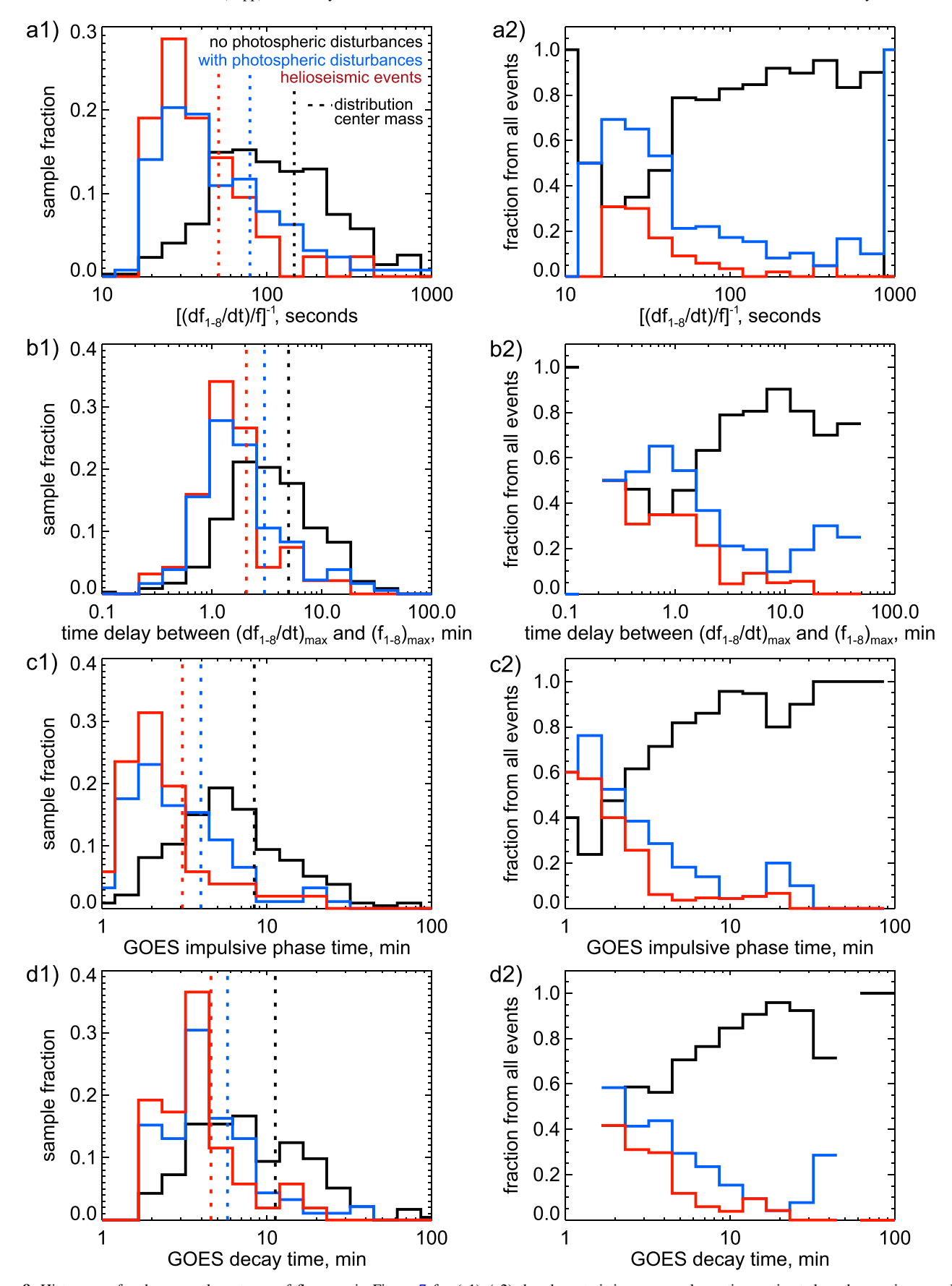


Figure 7. Histograms for three types of flares: (1) without photospheric perturbations (black lines), (2) with photospheric perturbations (blue) including sunquakes, and (3) with sunquakes (red). Left column shows the relationship between event occurrence within the types and the SXR flux (a1) and the maximum value of the SXR flux time derivative (b1). Right column shows probability functions that determine the event occurrence relative to the total number of all flares for the SXR flux (a2) and the maximum value of the SXR flux time derivative (b2).



**Figure 8.** Histograms for the same three types of flares as in Figure 7 for (a1)–(a2) the characteristic energy release time estimated as the maximum value of  $f_{1-8}/(df_{1-8}/dt)$ ; (b1)–(b2) for the time delays between the peak times of  $f_{1-8}$  and  $df_{1-8}/dt$ ; (c1)–(c2) the impulsive phase duration; and (d1)–(d2) the flare decay time.

shows the flare distributions versus the flare maximal SXR fluxes (panels (a1)–(a2)), and versus the maximum value of the SXR flux time derivative, which characterizes the maximal energy release rate (panels (b1)–(b2)). Left columns show the distributions of events in each of the three groups normalized to the total number of events in these groups as a function of the selected parameters (shown in the *x*-axis). The right column shows the occurrence rate of events within the three groups relative to the total number of flares (with and without photospheric perturbations). In other words, the panels in the right columns show probability functions. Value 1 means that all flares in the particular range  $\Delta X_i$  of a parameter represented by the *x*-axis are sunquakes, photospheric (including sunquakes) events, or events without sunquakes (indicated in red, blue, and black respectively).

These distributions show that the appearance of helioseismic waves is more probable for the flare of higher GOES X-ray classes with higher energy release rates. We can introduce a formal criterion for the appearance of the flare helioseismic response: with probability higher than 60% sunquakes will be registered when the maximal flare-energy release rate is higher than  $2 \times 10^{-7} \ \mathrm{W} \ \mathrm{m}^{-2} \ \mathrm{s}^{-1}$ .

Comparing the centers of mass calculated for the distributions (dashed lines in Figure 7(b1)), we determine that the seismic flares are six times more impulsive than the flares without photospheric impacts. If we consider all flares with photospheric perturbations (blue histograms) then we see only small differences compared to the histogram for the seismic flares (red lines). Nevertheless, we can state that the flares with photospheric impacts but without pronounced helioseismic waves are less impulsive but still have high-energy release rates than the flares without photospheric perturbations.

This leads us to a conclusion that the seismic flares are more impulsive than the nonseismic flares in terms of the maximal flare-energy release rate. To confirm the impulsive nature of the flares producing sunquakes, we made an additional comparative analysis of the three groups from the point of view of the characteristic energy release times.

Figure 8 presents distributions of the two types (similarly to Figure 7, sorted into two columns) illustrating differences between the characteristic flare times of the seismic and nonseismic flares. Panels (a1)-(a2) present the characteristic energy release time estimated as the maximum value of  $f_{1-8}/(df_{1-8}/dt)$ , where  $f_{1-8}$  is the GOES SXR flux in the 1-8 Å channel. Panels (b1)-(b2) show distributions of the time delays between the peak times of  $f_{1-8}$  and  $df_{1-8}/dt$ . Distributions of the impulsive phase duration defined as the time interval when the SXR flux was higher than  $\max(f_{1-8})/10$ are shown in panels (c1)-(c2). Panels (d1)-(d2) show the flare distribution for the SXR decay time determined as the time interval during which the SXR flux decreased by a factor of two from its maximum. We also calculated the centers of mass of the distributions for easier comparison among the flare classes. From these distributions, we find that the seismic flares are characterized by shorter durations compared to the nonseismic flares. In other words, sunquake events are more probable for flares that are more impulsive. This difference is more pronounced in terms of the maximum values of the SXR flux time derivative.

#### 5. Conclusions

We have performed a comprehensive search for seismically active (producing sunquakes) flares among all M-X class solar flares observed in Solar Cycle 24. Using the new catalog of sunquakes, we performed a comparative statistical analysis of the X-ray emission from the GOES data and its temporal dynamics for seismic and nonseismic flares. The obtained results can be summarized as follows:

- We have found that 94 flares among 507 flares of the X-ray class greater than M1.0 were seismically active. Our analysis has shown that there are many solar flares of moderate class with strong sunquakes, while in some powerful X-class flares, helioseismic waves were not observed or were weak.
- 2. Our analysis also revealed that during Solar Cycle 24, there were several active regions characterized by the most efficient generation of sunquakes.
- 3. We found that the sunquake total energy correlates with the maximum value of the soft X-ray time derivative better (with correlation coefficient ≈0.7) than with the X-ray class (contrary to what one could expect from the "big-flare syndrome" idea, Kahler 1982). In this case, the impulsiveness of the energy release plays an important role.
- 4. It was shown that the flares producing sunquakes are more impulsive (shorter flare times and higher heating rate) compared to the flares without photospheric perturbations. The most evident difference between distributions of the seismic and nonseismic flares appears in terms of the maximum values of the flare-energy release rate.

In the presented initial statistical study of the new sunquake catalog we investigated the relationship of the sunquake energetics with the temporal and amplitude characteristics of the flare soft X-ray emission. Although the results do not allow us to answer the long-standing question about the exact mechanism of the flare helioseismic response, they show that the impulsiveness of the flare-energy release characterized by the SXR flux derivative (the Neupert effect) plays an important role in the sunquake mechanism. The impulsive nature of seismic flares gives hints that they are compact with fast energy release rate. Thus, one can assume that low-lying short magnetic loops are involved in the flare-energy release process.

In our catalog, the helioseismic events are tagged to the standard GOES classification of solar flares in terms of the peak of soft X-ray emission. Our previous studies have shown that the sunquake initiation may occur at the very beginning of the flare impulsive phase (Sharykin et al. 2017), or during a subflare X-ray peak (Sharykin & Kosovichev 2015). Thus, further detailed studies considering characteristics of the magnetic field structure and flare emission in other ranges of electromagnetic spectrum are needed to shed more light on the sunquake mechanism.

The created catalog of helioseismic solar flares opens new opportunities for performing statistical analyses, as well as for in-depth research of individual cases. It will contribute to better understanding of the mechanism of sunquakes and flares.

The research was supported by the NASA Grants NNX14AB68G and NNX16AP05H, NSF grant 1916509, and grant of the President of the Russian Federation for the State Support of Young Russian Science PhDs (MK-5921.2018.2).

The research is also partially supported by the Russian Foundation of Basic Research (RFBR, grant 18-02-00507). The observational data are courtesy of the SDO/HMI and GOES science teams.

## ORCID iDs

Ivan N. Sharykin https://orcid.org/0000-0002-5719-2352 Alexander G. Kosovichev https://orcid.org/0000-0003-0364-4883

## References

```
Allred, J. C., Kowalski, A. F., & Carlsson, M. 2015, ApJ, 809, 104
Alvarado-Gómez, J. D., Buitrago-Casas, J. C., Martínez-Oliveros, J. C., et al.
   2012, SoPh, 280, 335
Aschwanden, M. J., Caspi, A., Cohen, C. M. S., et al. 2019, JPhCS, 1332,
Besliu-Ionescu, D., Donea, A., & Cally, P. 2017, SunGe, 12, 59
Bornmann, P. L., Speich, D., Hirman, J., et al. 1996, Proc. SPIE, 2812, 291
Brown, J. C. 1971, SoPh, 18, 489
Buitrago-Casas, J. C., Martínez Oliveros, J. C., Lindsey, C., et al. 2015, SoPh,
   290, 3151
Burtseva, O., Martínez-Oliveros, J. C., Petrie, G. J. D., & Pevtsov, A. A. 2015,
   ApJ, 806, 173
Chen, R. 2019, PhD thesis, Stanford Univ., https://searchworks.stanford.edu/
   view/13137617
Christensen-Dalsgaard, J., Proffitt, C. R., & Thompson, M. J. 1993, ApJL,
   403, L75
Dennis, B. R., & Zarro, D. M. 1993, SoPh, 146, 177
Donea, A. 2011, SSRv, 158, 451
Donea, A.-C., Braun, D. C., & Lindsey, C. 1999, ApJL, 513, L143
Fisher, G. H., Bercik, D. J., Welsch, B. T., & Hudson, H. S. 2012, SoPh,
  277, 59
Fisher, G. H., Canfield, R. C., & McClymont, A. N. 1985, ApJ, 289, 414
Hudson, H. S., Fisher, G. H., & Welsch, B. T. 2008, in ASP Conf. Ser. 383,
   Subsurface and Atmospheric Influences on Solar Activity, ed. R. Howe
   et al. (San Francisco, CA: ASP), 221
```

```
Kosovichev, A. G. 1986, BCrAO, 75, 6
Kosovichev, A. G. 2006, SoPh, 238, 1
Kosovichev, A. G. 2015, in Extraterrestrial Seismology, ed. V. Tong &
  R. García (Cambridge: Cambridge Univ. Press), 306
Kosovichev, A. G., & Sekii, T. 2007, ApJL, 670, L147
Kosovichev, A. G., & Zharkova, V. V. 1995, in ESA Special Publication 376,
  Helioseismology, ed. J. T. Hoeksema et al. (Paris: ESA), 341
Kosovichev, A. G., & Zharkova, V. V. 1998, Natur, 393, 317
Lin, R. P., Dennis, B. R., Hurford, G. J., et al. 2002, SoPh, 210, 3
Lindsey, C., & Braun, D. C. 1997, ApJ, 485, 895
Lindsey, C., & Braun, D. C. 2000, SoPh, 192, 261
Livshits, M. A., Badalian, O. G., Kosovichev, A. G., & Katsova, M. M. 1981,
   SoPh, 73, 269
Neupert, W. M. 1968, ApJL, 153, L59
Raja Bayanna, A., Kumar, B., Venkatakrishnan, P., et al. 2014, RAA, 14,
Russell, A. J. B., Mooney, M. K., Leake, J. E., & Hudson, H. S. 2016, ApJ,
Sadykov, V. M., Kosovichev, A. G., Kitiashvili, I. N., & Kerr, G. S. 2020, ApJ,
Scherrer, P. H., Bogart, R. S., Bush, R. I., et al. 1995, SoPh, 162, 129
Scherrer, P. H., Schou, J., Bush, R. I., et al. 2012, SoPh, 275, 207
Sharykin, I. N., & Kosovichev, A. G. 2015, ApJ, 808, 72
Sharykin, I. N., & Kosovichev, A. G. 2018, ApJ, 864, 86
Sharykin, I. N., Kosovichev, A. G., Sadykov, V. M., Zimovets, I. V., &
  Myshyakov, I. I. 2017, ApJ, 843, 67
Sharykin, I. N., Kosovichev, A. G., & Zimovets, I. V. 2015, ApJ, 807, 102
Stefan, J. T., & Kosovichev, A. G. 2019, arXiv:1911.06839
Sun, X., Hoeksema, J. T., Liu, Y., Kazachenko, M., & Chen, R. 2017, ApJ,
  839, 67
Wolff, C. L. 1972, ApJ, 176, 833
Zhao, H., & Chou, D.-Y. 2016, ApJ, 822, 23
Zhao, J., Parchevsky, K. V., & Kosovichev, A. G. 2012, in ASP Conf. Ser.
  462, Interaction of Helioseismic Waves with Sunspots: Observations and
  Numerical MHD Simulations, ed. H. Shibahashi, M. Takata, &
  A. E. Lynas-Gray (San Francisco, CA: ASP), 277
Zharkov, S., Green, L. M., Matthews, S. A., & Zharkova, V. V. 2011, ApJL,
  741, L35
Zharkov, S., Green, L. M., Matthews, S. A., & Zharkova, V. V. 2013, SoPh,
  284, 315
```

Kahler, S. W. 1982, JGR, 87, 3439